OPEN ACCESS

Condensed Matter Physics REPORT

Self-assembly and manipulation of Te clusters on WTe_2 surface

Zi-Yi Han,[1,3,5] Xinlei Zhao,[2,5] Ya-Xin Zhao,[1,3,5] Mo-Han Zhang,[1,3] Hui-Ying Ren,[1,3] Xiao-Feng Zhou,[1,3] Ruo-Han Zhang,[1,3] Chao Yan,[1,3] Ya-Ning Ren,[1,3,*] Yong Xu,[2,4,*] and Lin He[1,3,*]

*Correspondence: yning@mail.bnu.edu.cn (Y.R.); yongxu@mail.tsinghua.edu.cn (Y.X.); helin@bnu.edu.cn (L.H.)

Received: April 4, 2026; Accepted: July 4, 2026; Published Online: July 8, 2026; https://doi.org/10.59717/j.tip.2026.100008

GRAPHICAL ABSTRACT

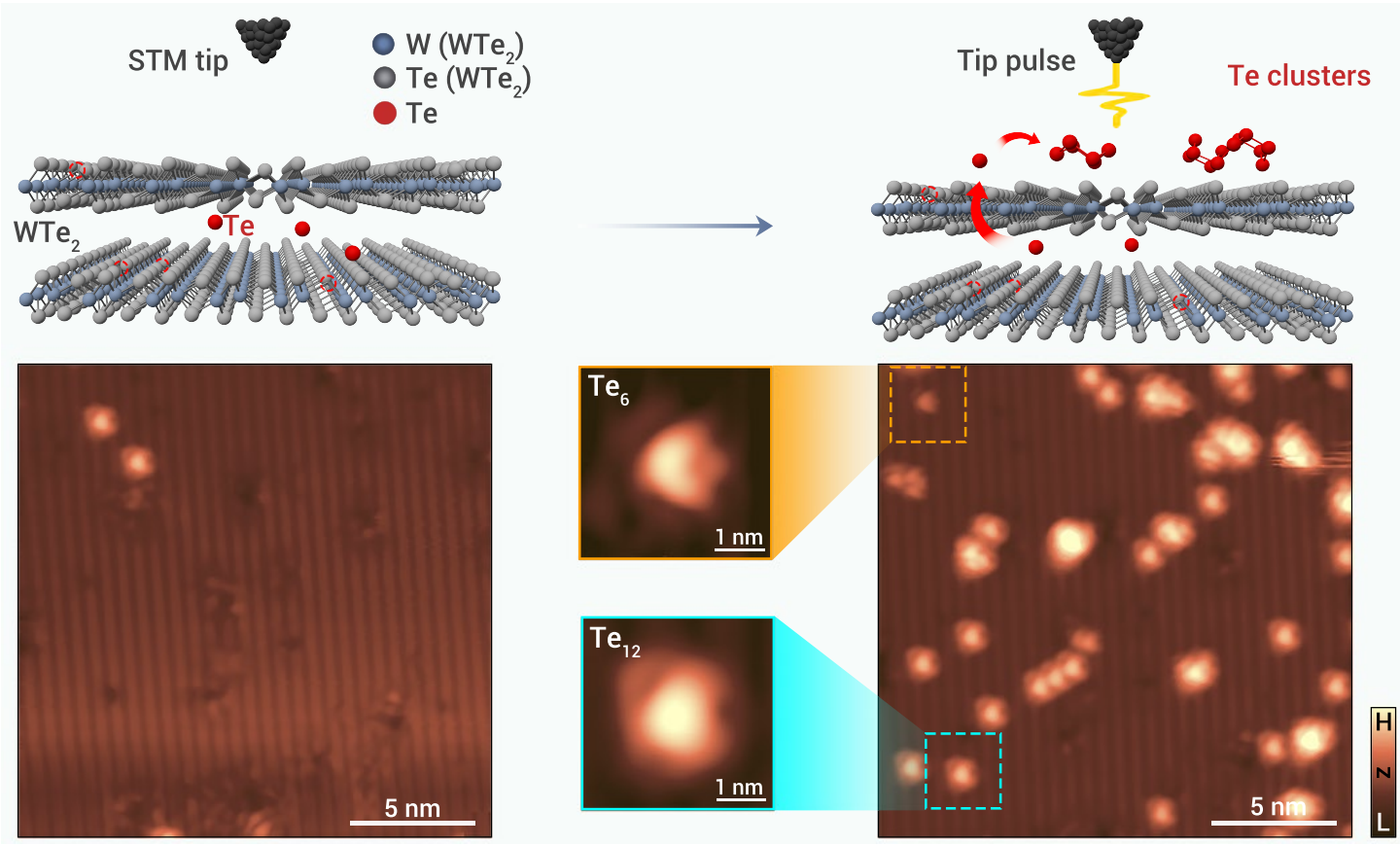

PUBLIC SUMMARY

- Self-assembly and tip manipulation are combined to construct atomically precise tellurium (Te) clusters.
- Ring-like Te clusters on 1T′-WTe_2 can be created, manipulated, and reshaped with atomic precision.
- This work opens new avenues for tailoring atomic-scale assemblies and exploring emergent quantum phenomena.

REPORT Condensed Matter Physics

Self-assembly and manipulation of Te clusters on WTe_2 surface

Zi-Yi Han,[1,3,5] Xinlei Zhao,[2,5] Ya-Xin Zhao,[1,3,5] Mo-Han Zhang,[1,3] Hui-Ying Ren,[1,3] Xiao-Feng Zhou,[1,3] Ruo-Han Zhang,[1,3] Chao Yan,[1,3] Ya-Ning Ren,[1,3,*] Yong Xu,[2,4,*] and Lin He[1,3,*]

[1]Center for Advanced Quantum Studies, School of Physics and Astronomy, Institute for Advanced Study, Beijing Normal University, Beijing 100875, China
[2]State Key Laboratory of Low Dimensional Quantum Physics and Department of Physics, Tsinghua University, Beijing 100084, China
[3]Key Laboratory of Multiscale Spin Physics (Beijing Normal University), Ministry of Education, Beijing 100875, China
[4]Frontier Science Center for Quantum Information, Beijing 100084, China
[5]These authors contributed equally
*Correspondence: yning@mail.bnu.edu.cn (Y.R.); yongxu@mail.tsinghua.edu.cn (Y.X.); helin@bnu.edu.cn (L.H.)

Received: April 4, 2026; Accepted: July 4, 2026; Published Online: July 8, 2026; https://doi.org/10.59717/j.tip.2026.100008

Citation: Han Z.-Y., Zhao X., Zhao Y.-X., et al. (2026). Self-assembly and manipulation of Te clusters on WTe_2 surface. *The Innovation Physics* **1**:100008.

The ability to build matter with atomic precision is central to nanoscience, with profound implications for engineering functional quantum materials and fabricating nanoscale devices. Two different methods, i.e., molecular self-assembly and atomic manipulation, are developed to achieve such a goal. Although both have advanced considerably, their integration within a single system remains largely unexplored, hampering the construction of more complex nanostructures with greater control. Here, we report a method to trigger self-assembly of Te clusters on 1T'-WTe_2 surface and show the ability to further manipulate the Te clusters via scanning tunnelling microscopy tip engineering. This enables us to change the position and number of atoms of the Te clusters with atomic precision. Our results indicate that the seamless combination of self-assembly and manipulation in a single system opens new avenues for constructing and tailoring atomic-scale architectures, providing an ideal platform with atomic precision to explore emergent quantum phenomena.

INTRODUCTION

The precise control and manipulation of matter at the atomic scale have long been central pursuits in nanoscience, offering profound insights into atomic interactions and enabling the design of novel quantum materials, molecular architectures, and next-generation microelectronic devices.[1–6] One promising strategy in this realm is molecular self-assembly, where atoms or molecules spontaneously organize into ordered structures driven by intrinsic interactions.[7–14] Complementarily, scanning probe techniques, such as scanning tunnelling microscopy (STM), offer the capability to directly manipulate individual atoms and molecules, providing an alternative approach to crafting atomic-scale systems.[15–23] Despite notable advancements in both self-assembly and atomic manipulation, the integration of these two processes within a single system remains largely unexplored. Combining the two strategies could pave the way for constructing more complex nanostructures with exceptional precision.

Here, we report the combination of self-assembly and manipulation of tellurium (Te) clusters on the surface of 1T'-WTe_2. Te, a chalcogen element with unique electronic properties, stands out for its strong spin-orbit coupling and versatile bonding capabilities.[24,25] Our experiments demonstrate that Te atoms spontaneously organize into clusters with a certain degree of structural uniformity on the 1T'-WTe_2 surface, in sharp contrast to noble metal clusters, whose lack of directional bonding typically leads to structural variability and complexity.[26–29] This inherent uniformity of Te assemblies provides a unique platform for bottom-up molecular design. Furthermore, we show that the position and number of atoms of these Te clusters can be changed by using an STM tip.

MATERIALS AND METHODS

Samples preparation

The high-quality 1T'-WTe_2 multilayers were prepared on silicon substrates using thermal release tape. First, a piece of 1T'-WTe_2 multilayers was picked up with the tape and attached to the silicon substrate. Next, the sample was placed silicon-side down on a hot plate preheated to 130 °C for less than 10 seconds. During this brief period, the tape lost its adhesion, allowing the WTe_2 multilayers to transfer successfully onto the silicon substrate. Finally, the sample was annealed at 300 °C for 5.5 hours.

STM and STS measurements

STM/STS measurements were conducted at low temperature (77 K) and under ultrahigh vacuum (~ 10^{-10} Torr) using the USM-1300 scanning probe microscope (77 K) from UNISOKU. The tips were prepared by chemical etching from a tungsten wire. Differential conductance (d*I*/d*V*) measurements were performed using a standard lock-in technique with an ac bias modulation of 5 mV and a 793 Hz signal added to the tunnelling bias.

Theoretical methods

First-principles calculations were performed using density functional theory (DFT) implemented within the Vienna *ab initio* simulation package (VASP)[44,45] employing the projector augmented wave (PAW)[46,47] pseudopotential approach. The generalized gradient approximation (GGA) with the Perdew-Burke-Ernzerhof type was adopted for the exchange-correlation potential.[48] A plane-wave basis set with an energy cutoff of 400 eV was adopted to ensure the accuracy of the electronic structure calculations. A Gaussian smearing of 0.05 eV was adopted for the Fermi surface broadening. The Te_6 cluster simulations employed a 6×3 WTe_2 supercell, whereas the Te_{12} system utilized a 10×5 supercell configuration. The Γ-centered k-meshes of 6×6×1 and 4×4×1 were implemented for Brillouin zone integrations in the 6×3 and 10×5 supercells, respectively. The thickness of the vacuum along the *z*-direction was set to > 12 Å. The atomic positions were relaxed until Hellmann-Feynman forces were smaller than 0.01eV/Å^{-1}. The STM topographic images were numerically generated through post-processing of the local density of states (LDOS) derived from our DFT calculations. Employing the Tersoff-Hamann approximation,[49,50] the constant-current mode images were constructed by calculating iso-surfaces of the integrated LDOS at a tip-sample separation of about 1.5 Å above the surface Te clusters.

RESULTS

Formation of Te vacancies and intercalated Te atoms

The 1T'-WTe_2 crystal is composed of Te-W-Te atomic layers in a sandwich-like structure (Figure 1A). Te vacancies form more readily than W vacancies in the 1T'-WTe_2 due to their lower formation energy,[30,31] enabling controlled defect creation through thermal annealing.[32,33] After annealing at 300 °C for 5.5 hours, a high concentration of Te vacancies, visible as dark spots in a representative large-scale STM image (Figure 1B), emerges on the WTe_2 surface. An enlarged view of a representative vacancy (Figure 1C) agrees well with that reported previously[31] and also aligns with a simulated Te vacancy image (Figure 1D), confirming its identification as a Te vacancy explicitly. A defect density of ~ 5.6 × 10^{12} cm^{-2} in the studied region of the topmost layer is roughly estimated according to the STM measurements.

The high-density Te vacancies generated during the annealing process simultaneously result in amounts of released Te atoms, which serve as fundamental units for molecular assembly. However, at elevated temperatures, surface Te atoms tend to aggregate into large clusters due to thermal diffusion. In our experiment, the layered WTe_2 has a natural advantage to mitigate this because a fraction of the released Te atoms will intercalate between the WTe_2 layers,[32] preventing excessive aggregation. These intercalated Te atoms form a hidden reservoir that offers access to individual Te atom and facilitates precise studies of atomic-scale assembly. In our experiment, by taking advantage of the high mobility[34] of these intercalated Te atoms, we demonstrate that they can be selectively extracted with STM tip

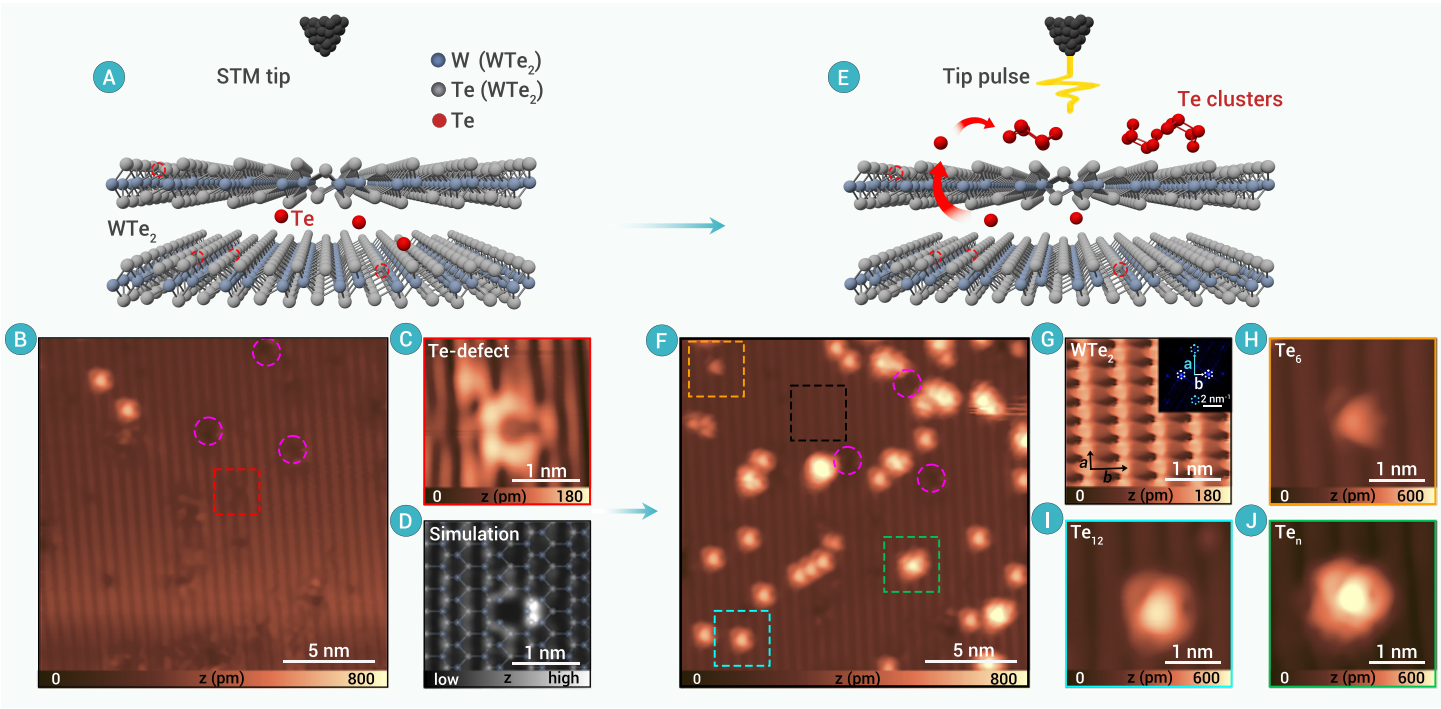

Figure 1. Atomic-precision self-assembly of Te clusters on the 1T'-WTe_2 surface (A and E) Schematic illustrations of Te cluster formation on the 1T'-WTe_2 surface. (B and F) Large-scale topographic images of the WTe_2 surface before and after tip pulse (V = 1.5 V, τ = 10 ms), respectively. Pink dashed circles mark the same set of Te defects to serve as position references. Orange, blue, and green dashed boxes highlight Te clusters composed of 6, 12, and n Te atoms (n > 12), respectively. Scanning parameters: V_b = 0.75 V, I = 200 pA for panel (B), and V_b = 0.8 V, I = 150 pA for panel (F). (C) Magnified view of the Te defect outlined by the red dashed box in panel (B). Scanning parameters: V_b = 0.12 V, I = 50 pA. (D) Simulated STM image of the Te defect. (G) Atomic-resolution image of the WTe_2 substrate corresponding to the black dashed box in panel (F), confirming the structural integrity of the WTe_2 substrate during the STM tip pulsing process. Scanning parameters: V_b = 0.6 V, I = 100 pA. Inset: corresponding fast Fourier transform (FFT) image. (H)-(J) Magnified view of Te_6, Te_{12} and Te_n clusters, corresponding to orange, blue, and green dashed boxes in panel (F), respectively. Scanning parameters: V_b = 0.8 V, I = 100 pA for panel (H), V_b = 0.8 V, I = 70 pA for panel (I), and V_b = 0.25 V, I = 70 pA for panel (J).

pulses. We positioned the tip above the annealed WTe_2 surface while maintaining a bias voltage of 750 mV and a tunnelling current of 100 pA. By applying STM tip pulses (V = 1.5 V, τ = 10 ms), we observe the formation of Te clusters on the WTe_2 surface. This phenomenon is attributable to transient Joule heating generated by the tip pulses, which locally elevates the temperature above the diffusion barrier, thereby enabling the selective excitation of intercalated Te atoms.[35,36] The low interlayer diffusion barrier (~ 0.44 eV) drives these atoms to migrate from the interlayers onto the WTe_2 surface, as schematically illustrated in Figure 1E. Crucially, the low-temperature environment in our experiment suppresses Te's high in-plane mobility[34] and avoids excessive clustering of the Te atoms. This provides an exceptional platform for probing atomic-scale self-assembly and manipulation with high precision.

Self-assembly of Te_6 clusters

Once extracted onto the surface, the Te atoms exhibit remarkable self-assembly behavior (Figures 1F-J), driven by their high surface mobility and the relatively low diffusion barrier (~ 0.62 eV).[34] Under these conditions, Te atoms spontaneously form stable cluster structures, with the final configurations governed by thermodynamic equilibrium. Experimentally, we observe a large number of Te clusters, and the substantial population facilitates the experimental determination of precise cluster structures, similar in concept to mass-selective deposition of metal clusters studied in catalysis.[27-29] Analysis of the resulting clusters reveals a certain degree of uniformity, suggesting the formation of distinct cluster species with an identical number of atoms and geometries (Figure 1F, see Figure S1A for a larger image).

Detailed size-distribution analysis reveals three predominant cluster configurations: (i) The smallest observed species consists of six Te atoms arranged in a compact structure (Te_6) (Figure 1H), accounting for approximately 10% of the total cluster population; (ii) The most abundant species, comprising about 70% of the population, is a 12-atom structure (Te_{12}), forming a highly symmetric arrangement (Figure 1I); (iii) Finally, the largest species observed contains n Te atoms (Te_n), with n larger than 12, assembling into a more complex and extended configuration (Figure 1J). Similar distributions are consistently observed across multiple independent datasets (Figure S1). This distinct categorization of cluster species underscores the intricate interplay between interatomic forces and surface diffusion in dictating the self-assembly process.

To elucidate the structural origin of the experimentally observed clusters, we focus on the smallest Te cluster as a representative example (see details in Methods). Chalcogen atoms, such as Te, tend to form low-dimensional ring or chain structures due to the strong sp hybridized orbitals, giving rise to σ- and π-bonding between neighboring atoms.[25,37-40] Consistent with this tendency, first-principles calculations for free-standing Te clusters with different atomic numbers show a clear preference for ring-like geometries (Figure S2). When the WTe_2 substrate is included, Te_6 is predicted to be the most energetically favorable species (Note S1 & Table S1). To determine the most stable configuration of Te_6 on the WTe_2 surface, we systematically explore various high-symmetry adsorption sites, including top, bridge, and hollow sites (Figure S3), while considering different geometries and their rotated counterparts, generating a total of 60 possible configurations. After structural optimization, all low-energy configurations converge to a buckled hexagonal ring (Figures 2A-B). This is consistent with the reported lowest-energy structure of chalcogen hexamers in the previous theoretical study,[25] even though no substrate was taken into account.

The hexagonal Te_6 structure is further validated through simulated STM images based on the Tersoff-Hamann approximation (Figures S4-5). At a bias voltage V_b of 0.45 V, the calculated image at E = -0.45 eV faithfully reproduces the key features observed in the experimental STM topography (Figures 2C-D). Specifically, the lower-layer Te atoms exhibit an approximate threefold symmetry, while a pronounced local intensity enhancement appears on the side hosting the slightly elevated Te atom (left side), in good agreement with the experimental observations (see Figure S5 for additional energies). The apparent inversion between experimental bias voltages and calculated energies in Figure 2 may arise from strong coupling between the STM tip and the cluster[41] (Figure 2E, see Note S2 and Figure S6 for further discussion). To probe the electronic structure of Te_6 cluster more directly, we perform scanning tunnelling spectroscopy (STS). The experimental dI/dV spectra exhibit a series of well-defined resonances, indicative of discrete

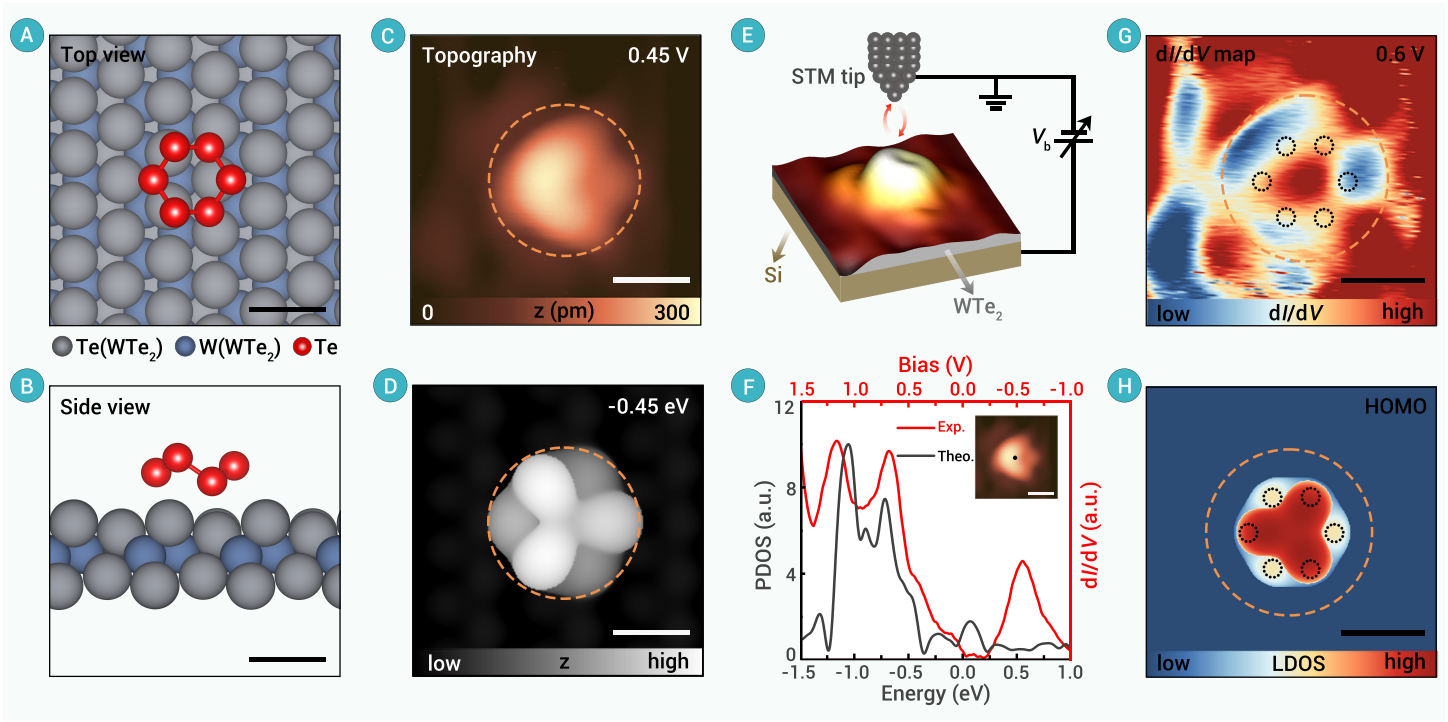

Figure 2. Atomic structure and electronic state distribution of Te_6 cluster (A and B) Top and side views of the atomic model of the Te_6 cluster, showing its buckled hexagonal ring structure. (C) STM topographic image of the Te_6 cluster at V_b = 0.45 V. Scanning parameters: V_b = 0.45 V, I = 100 pA. (D) Simulated STM image of the Te_6 cluster at E = -0.45 eV. (E) Schematic of the experimental STM set-up, in which the tip-cluster coupling is denoted by double-ended red arrows. (F) Calculated PDOS and experimental STS spectrum of Te_6 cluster. The black line corresponds to the PDOS of Te_6 cluster, which has been shifted by +0.3 eV, and the red line represents the STS spectrum acquired at the location marked in the inset. (G) The dI/dV map of the Te_6 cluster acquired at V_b = 0.6 V. Scanning parameters: V_b = 0.6 V, I = 150 pA. (H) Calculated HOMO local density of states (LDOS) map taken 0.2 nm below the free-standing Te_6 cluster, where strong tip–cluster coupling makes the substrate effectively act as the "tip". The black circles in panels (G) and (H) indicate the positions of the atoms in the Te_6 cluster. The orange dashed circles in panels (C), (D), (G), and (H) represent the same size. The scale bar is 0.5 nm.

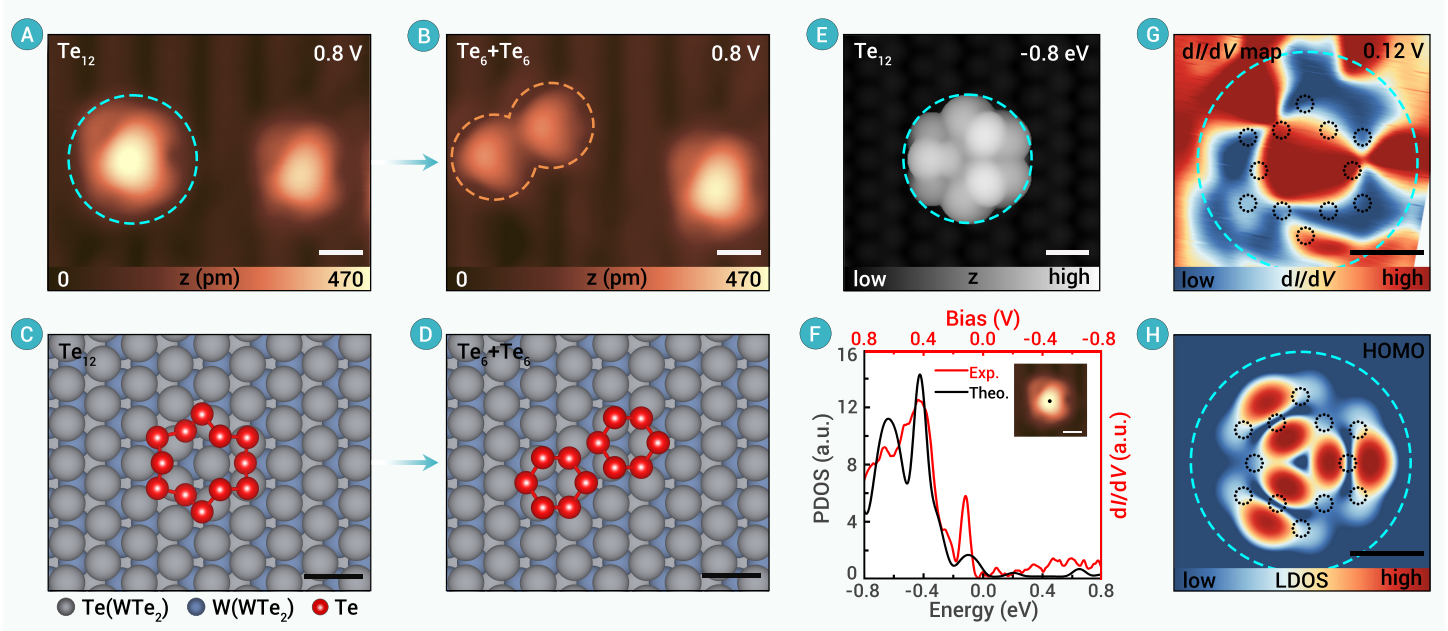

Figure 3. Atomic structure and electronic state distribution of the Te_{12} cluster (A and B) STM topographic images of a Te_{12} cluster before (A) and after (B) tip manipulation, demonstrating the splitting of the Te_{12} cluster. Scanning parameters: V_b = 0.8 V, I = 150 pA for panel (A), and V_b = 0.8 V, I = 100 pA for panel (B). (C and D) Atomic models of the clusters within the blue dashed line in panel (A) and orange dashed line in panel (B), showing the splitting of one Te_{12} cluster into two Te_6 clusters. (E) Simulated STM image of the Te_{12} cluster at E = -0.8 eV. (F) Calculated PDOS and experimental STS spectrum of Te_{12} cluster. The black line corresponds to the PDOS of Te_{12} cluster, which has been shifted by +0.2 eV, and the red line represents the STS spectrum acquired at the location marked in the inset. (G) The dI/dV map taken for the Te_{12} cluster at V_b = 0.12 V. Scanning parameters: V_b = 0.12 V, I = 50 pA. (H) Simulated HOMO LDOS map taken 0.2 nm below the free-standing Te_{12} cluster. The black circles in panels (G) and (H) indicate the positions of the atoms in the Te_{12} cluster. The blue dashed circles in panels (A), (E), (G), and (H) represent the same size. The scale bar is 0.5 nm.

electronic states associated with a cluster (Figure 2F). First-principles calculations incorporating the WTe_2 substrate further substantiate these observations. Analysis of the projected density of states (PDOS) for Te_6 cluster reveals discrete energy levels that match the experimentally measured STS spectra once the energy inversion effect is taken into account (Figure 2F). We further examine the spatial character of these electronic states by mapping their real-space distribution. Comparison of the experimental dI/dV map acquired at V_b = 0.6 V with the calculated highest occupied molecular orbital

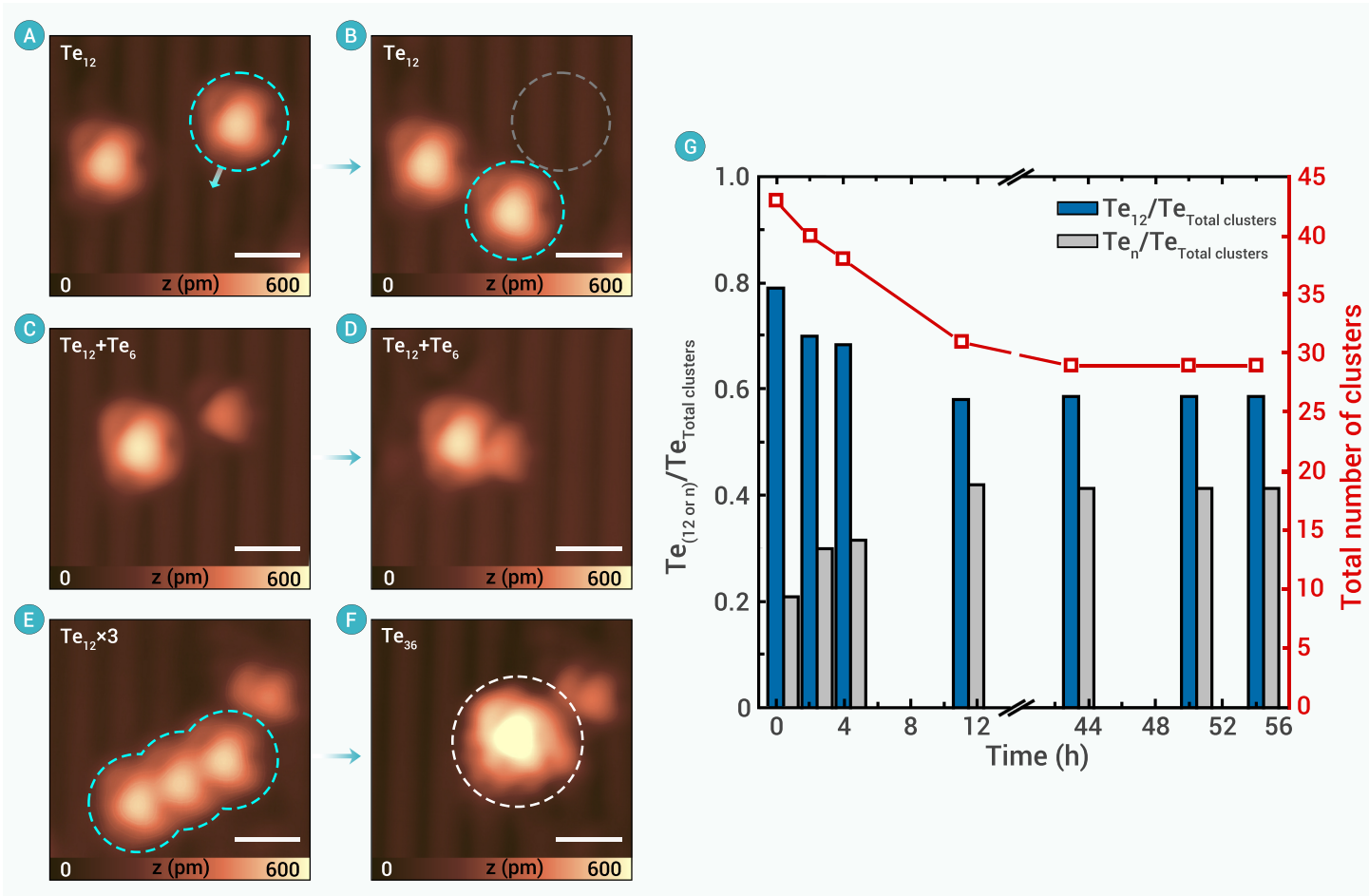

Figure 4. STM tip manipulation of Te clusters (A and B) STM topographic images of a Te_{12} cluster before (A) and after (B) being moved by the STM tip. Scanning parameters: V_b = 0.75 V, I = 50 pA, and V_b = 0.8 V, I = 50 pA, respectively. (C and D) STM topographic images of a Te_{12} cluster and a Te_6 cluster before (C) and after (D) spatially gathering. Scanning parameters: V_b = 1 V, I = 150 pA for both images. (E and F) STM topographic images of three Te_{12} clusters before (E) and after (F) merging. The white circle in panel (F) highlights the Te_{36} cluster formed by merging. Scanning parameters: V_b = 0.8 V, I = 150 pA, and V_b = 0.75 V, I = 50 pA, respectively. (G) Time dependence of the percentage of Te_{12} and larger Te_n (n > 12) clusters within the same area (Figure S12). All images are acquired with the STM tip positioned at a relatively large tip–sample separation (V_b = 0.8 V, I = 100 pA), minimizing direct tip-induced manipulation. After being initially formed, the clusters gradually assemble into larger structures, eventually reaching energetic equilibrium. The scale bar is 1 nm.

(HOMO) demonstrates a consistent threefold-symmetric charge distribution (Figures 2G-H), providing additional support for the proposed structural and electronic model (see Figure S7 for additional energies). The discrepancy between the experimental observations and theoretical predictions may partially stem from the fact that the calculation of the PDOS assumes a constant-height mode, whereas the dI/dV measurements are performed in a constant-current mode. Notably, the ring-like structure of the Te_6 remains largely preserved upon adsorption on the WTe_2 substrate (Figures S2 & S5), with only a slight expansion of the Te-Te bond length (2.765 Å on the WTe_2 and 2.751 Å in the free-standing cluster), indicating weak electronic coupling between the cluster and the substrate. This structural robustness, along with the agreement between experimental and simulated results, underscores the stability of the Te_6 cluster and highlights its potential as a building block for more complex cluster assemblies.

Formation of Te_{12} clusters

Having established the structural and electronic properties of the Te_6, we next investigate the formation and characteristics of the Te_{12} clusters, the most abundant cluster-assembly observed. The number of Te atoms of the cluster, i.e., 12, is determined based on the fact that a Te_{12} cluster can be split into two Te_6 units by approaching the STM tip to the Te_{12} cluster (bias voltage V_b ~ 200 mV, current I ~ 200 pA) and sweeping across its center repeatedly (Figures 3A-D). This observation hints at a hierarchical self-assembly process, where smaller stable units serve as building blocks for larger cluster species. To gain further insight into the structure of Te_{12} cluster, we perform theoretical simulations, generating 10 composite systems by placing a 12-membered buckled ring structure at various high-symmetry adsorption sites on the WTe_2 surface. After structural relaxation, these configurations largely preserve their initial 12-membered ring morphologies (Figures 3C & S8A-B). Notably, similar buckled ring structures have also been predicted for other chalcogen elements.[39,40]

Energetically, the Te_{12} exhibits enhanced thermodynamic stability over the Te_6, as evidenced by its lower per-atom energy (Figure S2H). This energy reduction rationalizes the experimental observation that the Te_{12} is more prevalent than Te_6. Consistent with this structural model, simulated STM images at the reversed energies based on the Tersoff-Hamann approach show agreement with experimental results, reproducing (i) a nearly threefold symmetry in the upper-layer atoms and (ii) enhanced brightness on the side where the atoms are slightly elevated (right side) (Figures 3A & E, see Figure S8 for additional energies). These results provide further support for the proposed Te_{12} configuration. Mirroring the Te_6 case, the reversed energy between experimental and simulated images is attributed to strong tip-cluster coupling.

Beyond the structural agreement, a pronounced consistency is also observed in the electronic properties. As shown in Figure 3F, after considering the energy inversion induced by strong tip-cluster coupling, the experimental dI/dV spectrum shows close correspondence with the theoretically PDOS of the Te_{12} cluster. Furthermore, dI/dV mapping performed at the resonance energy of 0.12 V reveals a clear threefold-symmetric charge distribution in real space, which matches that of the calculated HOMO of the Te_{12} cluster (Figures 3G-H, see Figure S9 for additional energies). The enhanced intensity at the center of the experimental dI/dV map compared with the

simulated image is attributed to contributions from the underlying substrate.

Manipulation of Te clusters via STM Tip

Building on our understanding of the structural and electronic properties of the Te_6 and the Te_{12}, we further explore the dynamic manipulation of these Te clusters using the STM tip, revealing precise control over their assembly and evolution. By positioning the STM tip above individual Te clusters and scanning their surface at approximately 100 nm/s while maintaining a bias voltage of 200 mV and a tunnelling current of 200 pA, we achieve selective relocation of the clusters across the WTe_2 substrate without altering their internal crystalline structure (Figures 4A-D & S10). This controlled mobility further underscores the weak interaction between the clusters and the underlying surface, enabling fine-tuned manipulation at the atomic scale.

Notably, when the Te clusters are brought into proximity, their atoms spontaneously reorganize, forming larger clusters (Figures 4E-F & S11). This behavior hints at an intrinsic self-assembly mechanism driven by interatomic interactions, suggesting a pathway for constructing more complex cluster architectures through STM manipulation. To gain deeper insight into the evolution of these cluster assemblies, we track the changes in cluster populations over time by comparing STM scans of the same area (Figures 4G & S12). Initially, the density of Te clusters is measured as 6.9×10^{12} cm^{-2}. However, after 54 hours, the density significantly decreases to about 4.7×10^{12} cm^{-2}, indicating that the clusters have undergone reorganization. Importantly, the population of the Te_{12} clusters diminishes while larger clusters become more prevalent (Figure 4G), suggesting a thermodynamically driven process from an energetically metastable population toward a more stable distribution. Such a result further demonstrates that our low-temperature environment plays a vital role not only in avoiding excessive clustering of Te atoms, but also in in-situ creating and manipulating atomically precise clusters, offering a level of programmable control beyond spontaneous cluster formation under external perturbations in conventional Te-based systems.[42,43]

CONCLUSION

In summary, we demonstrate a synergistic approach that combines atomic-scale self-assembly and precise manipulation to engineer tellurium-based cluster architectures on the 1T'-WTe_2 surface. The Te atoms spontaneously form stable species like Te_6 and Te_{12}, serving as building blocks for hierarchical assembly. STM enables controlled manipulation, guiding the evolution of complex structures with atomic precision. This interplay not only reveals the fundamental mechanisms driving Te-based nanostructures but also offers a powerful platform for designing tailored quantum materials at the atomic scale.

REFERENCES

1. Barth J. V., Costantini G. and Kern K. (2005). Engineering atomic and molecular nanostructures at surfaces. *Nature* **437**:671–679. DOI:10.1038/nature04166
2. He Y., Gorman S. K., Keith D. et al. (2019). A two-qubit gate between phosphorus donor electrons in silicon. *Nature* **571**:371–375. DOI:10.1038/s41586-019-1381-2
3. Chou C.-W., Kurz C., Hume D. B. et al. (2017). Preparation and coherent manipulation of pure quantum states of a single molecular ion. *Nature* **545**:203–207. DOI:10.1038/nature22338
4. Imre A., Csaba G., Ji L. et al. (2006). Majority logic gate for magnetic quantum-dot cellular automata. *Science* **311**:205–208. DOI:10.1126/science.1120506
5. Yan H., Lin Y., Wu H. et al. (2017). Bottom-up precise synthesis of stable platinum dimers on graphene. *Nat. Commun.* **8**:1070. DOI:10.1038/s41467-017-01259-z
6. Kalff F. E., Rebergen M. P., Fahrenfort E. et al. (2016). A kilobyte rewritable atomic memory. *Nat. Nanotechnol.* **11**:926–929. DOI:10.1038/nnano.2016.131
7. Piquero-Zulaica I., Lobo-Checa J., Abd El-Fattah Z. M. et al. (2022). Engineering quantum states and electronic landscapes through surface molecular nanoarchitectures. *Rev. Mod. Phys.* **94**:045008. DOI:10.1103/RevModPhys.94.045008
8. Grill L., Dyer M., Lafferentz L. et al. (2007). Nano-architectures by covalent assembly of molecular building blocks. *Nat. Nanotechnol.* **2**:687–691. DOI:10.1038/nnano.2007.346
9. Chen Q., Bae S. C. and Granick S. (2011). Directed self-assembly of a colloidal kagome lattice. *Nature* **469**:381–384. DOI:10.1038/nature09713
10. Shang J., Wang Y., Chen M. et al. (2015). Assembling molecular Sierpiński triangle fractals. *Nat. Chem.* **7**:389–393. DOI:10.1038/nchem.2211
11. Chen J., Zhu E., Liu J. et al. (2018). Building two-dimensional materials one row at a time: Avoiding the nucleation barrier. *Science* **362**:1135–1139. DOI:10.1126/science.aau4146
12. Zhang Y.-Q., Paszkiewicz M., Du P. et al. (2018). Complex supramolecular interfacial tessellation through convergent multi-step reaction of a dissymmetric simple organic precursor. *Nat. Chem.* **10**:296–304. DOI:10.1038/nchem.2924
13. Montis R., Fusaro L., Falqui A. et al. (2021). Complex structures arising from the self-assembly of a simple organic salt. *Nature* **590**:275–278. DOI:10.1038/s41586-021-03194-y
14. Fang H., Mahalingam H., Li X. et al. (2023). Atomically precise vacancy-assembled quantum antidots. *Nat. Nanotechnol.* **18**:1401–1408. DOI:10.1038/s41565-023-01495-z
15. Crommie M. F., Lutz C. P. and Eigler D. M. (1993). Confinement of electrons to quantum corrals on a metal surface. *Science* **262**:218–220. DOI:10.1126/science.262.5131.218
16. Kim H. W., Han M., Shin H.-J. et al. (2011). Control of molecular rotors by selection of anchoring sites. *Phys. Rev. Lett.* **106**:146101. DOI:10.1103/PhysRevLett.106.146101
17. Gomes K. K., Mar W., Ko W. et al. (2012). Designer Dirac fermions and topological phases in molecular graphene. *Nature* **483**:306–310. DOI:10.1038/nature10941
18. Fölsch S., Martínez-Blanco J., Yang J. et al. (2014). Quantum dots with single-atom precision. *Nat. Nanotechnol.* **9**:505–508. DOI:10.1038/nnano.2014.129
19. Slot M. R., Gardenier T. S., Jacobse P. H. et al. (2017). Experimental realization and characterization of an electronic Lieb lattice. *Nat. Phys.* **13**:672–676. DOI:10.1038/nphys4105
20. Drost R., Ojanen T., Harju A. et al. (2017). Topological states in engineered atomic lattices. *Nat. Phys.* **13**:668–671. DOI:10.1038/nphys4080
21. Khajetoorians A. A., Wegner D., Otte A. F. et al. (2019). Creating designer quantum states of matter atom-by-atom. *Nat. Rev. Phys.* **1**:703–715. DOI:10.1038/s42254-019-0108-5
22. Chen I. J., Aapro M., Kipnis A. et al. (2022). Precise atom manipulation through deep reinforcement learning. *Nat. Commun.* **13**:7499. DOI:10.1038/s41467-022-35149-w
23. Sierda E., Huang X., Badrtdinov D. I. et al. (2023). Quantum simulator to emulate lower-dimensional molecular structure. *Science* **380**:1048–1052. DOI:10.1126/science.adf2685
24. Calavalle F., Suárez-Rodríguez M., Martín-García B. et al. (2022). Gate-tuneable and chirality-dependent charge-to-spin conversion in tellurium nanowires. *Nat. Mater.* **21**:526–532. DOI:10.1038/s41563-022-01211-7
25. Ghosh P., Bhattacharjee J. and Waghmare U. V. (2008). The origin of stability of helical structure of tellurium. *J. Phys. Chem. C* **112**:983–989. DOI:10.1021/jp077070d
26. Li X., Mitchell S., Fang Y. et al. (2023). Advances in heterogeneous single-cluster catalysis. *Nat. Rev. Chem.* **7**:754–767. DOI:10.1038/s41570-023-00540-8
27. Hu K.-J., Plant S. R., Ellis P. R. et al. (2015). Atomic resolution observation of a size-dependent change in the ripening modes of mass-selected Au nanoclusters involved in CO oxidation. *J. Am. Chem. Soc.* **137**:15161–15168. DOI:10.1021/jacs.5b08720
28. Li Z., Chen H.-Y. T., Schouteden K. et al. (2020). Unraveling the atomic structure, ripening behavior, and electronic structure of supported Au_{20} clusters. *Sci. Adv.* **6**:eaay4289. DOI:10.1126/sciadv.aay4289
29. Bonanni S., Aït-Mansour K., Harbich W. et al. (2012). Effect of the TiO_2 reduction state on the catalytic CO oxidation on deposited size-selected Pt clusters. *J. Am. Chem. Soc.* **134**:3445–3450. DOI:10.1021/ja2098854
30. Haldar S., Vovusha H., Yadav M. K. et al. (2015). Systematic study of structural, electronic, and optical properties of atomic-scale defects in the two-dimensional transition metal dichalcogenides MX_2 (M = Mo, W; X = S, Se, Te). *Phys. Rev. B* **92**:235408. DOI:10.1103/PhysRevB.92.235408
31. Zhao Y.-X., Jin H., Han Z.-Y. et al. (2025). Realization of fractional-layer transition metal dichalcogenides. *Nat. Commun.* **16**:3659. DOI:10.1038/s41467-025-59007-7
32. Lu W., Zhang Y., Zhu Z. et al. (2016). Thin tungsten telluride layer preparation by thermal annealing. *Nanotechnology* **27**:414006. DOI:10.1088/0957-4484/27/41/414006
33. Blades W. H., Frady N. J., Litwin P. M. et al. (2020). Thermally induced defects on WSe_2. *J. Phys. Chem. C* **124**:15337–15346. DOI:10.1021/acs.jpcc.0c04440
34. Evans P. E., Wang Y., Sushko P. V. et al. (2023). Understanding palladium-tellurium cluster formation on WTe_2: From a kinetically hindered distribution to thermodynamically controlled monodispersity. *PNAS Nexus* **2**:pgad212. DOI:10.1093/pnasnexus/pgad212
35. Sugawara K., Gotoh T. and Tanaka K. (2004). Nanoscale phase change in telluride films induced with scanning tunneling microscopes. *Jpn. J. Appl. Phys.* **43**:L676. DOI:10.1143/JJAP.43.L676
36. Ren Y.-N., Zhang M.-H., Zhou X.-F. et al. (2024). In situ creation and tailoring of interfacial quantum dots in graphene/transition metal dichalcogenide heterostructures. *Phys. Rev. B* **110**:125416. DOI:10.1103/PhysRevB.110.125416
37. Degtyareva O., Gregoryanz E., Somayazulu M. et al. (2005). Novel chain structures in group VI elements. *Nat. Mater.* **4**:152–155. DOI:10.1038/nmat1294
38. Jin Y., Maroulis G., Kuang X. et al. (2015). Geometries, stabilities and fragmental channels of neutral and charged sulfur clusters: S_n^Q (n = 3-20, Q = 0, ±1). *Phys. Chem. Chem. Phys.* **17**:13590–13597. DOI:10.1039/C5CP00728C
39. Millefiori S. and Alparone A. (2001). Ab initio study of the structure and polarizability of sulfur clusters, S_n (n = 2-12). *J. Phys. Chem. A* **105**:9489–9497. DOI:10.1021/jp0121466
40. Alexander A. D. and Otto F. S. (2001). Theory of zeolite supralattices: Se in zeolite Linde type A. *J. Phys.: Condens. Matter* **13**:10433. DOI:10.1088/0953-8984/13/46/

313
41. Guo J., Meng X., Chen J. et al. (2014). Real-space imaging of interfacial water with submolecular resolution. *Nat. Mater.* **13**:184–189. DOI:10.1038/nmat3848
42. Kowalczyk H., Biscaras J., Pistawala N. et al. (2023). Gate and temperature driven phase transitions in few-layer $MoTe_2$. *ACS Nano* **17**:6708–6718. DOI:10.1021/acsnano.2c12610
43. Pawbake A., Bellin C., Paulatto L. et al. (2019). Pressure-induced phase transitions in germanium telluride: Raman signatures of anharmonicity and oxidation. *Phys. Rev. Lett.* **122**:145701. DOI:10.1103/PhysRevLett.122.145701
44. Kresse G. and Furthmüller J. (1996). Efficiency of ab-initio total energy calculations for metals and semiconductors using a plane-wave basis set. *Comput. Mater. Sci.* **6**:15–50. DOI:10.1016/0927-0256(96)00008-0
45. Kresse G. and Furthmüller J. (1996). Efficient iterative schemes for *ab initio* total-energy calculations using a plane-wave basis set. *Phys. Rev. B* **54**:11169–11186. DOI:10.1103/PhysRevB.54.11169
46. Blöchl P. E. (1994). Projector augmented-wave method. *Phys. Rev. B* **50**:17953–17979. DOI:10.1103/PhysRevB.50.17953
47. Kresse G. and Joubert D. (1999). From ultrasoft pseudopotentials to the projector augmented-wave method. *Phys. Rev. B* **59**:1758–1775. DOI:10.1103/PhysRevB.59.1758
48. Perdew J. P., Burke K. and Ernzerhof M. (1996). Generalized gradient approximation made simple. *Phys. Rev. Lett.* **77**:3865–3868. DOI:10.1103/PhysRevLett.77.3865
49. Tersoff J. and Hamann D. R. (1983). Theory and application for the scanning tunneling microscope. *Phys. Rev. Lett.* **50**:1998–2001. DOI:10.1103/PhysRevLett.50.1998
50. Tersoff J. and Hamann D. R. (1985). Theory of the scanning tunneling microscope. *Phys. Rev. B* **31**:805–813. DOI:10.1103/PhysRevB.31.805

FUNDING AND ACKNOWLEDGMENTS

This work was supported by the National Natural Science Foundation of China (12425405, 12404198, 125B2080, 12334003, 12421004, 12361141826), National Key R and D Program of China (2021YFA1400100, 2021YFA1401900, 2024YFA1409100), "the Fundamental Research Funds for the Central Universities" (310400209521), the China National Postdoctoral Program for Innovative Talents (BX20240040), the China Postdoctoral Science Foundation (2023M740296, 2023TQ0174, 2024M761599), the Basic Science Center Project of NSFC (52388201), Fundamental and Interdisciplinary Disciplines Breakthrough Plan of the Ministry of Education of China (JYB2025XDXM408), the Postdoctoral Fellowship Program of CPSF (GZC20231369), and Beijing Key Laboratory of Quantum AI. The calculations were performed at National Supercomputer Center in Tianjin using the Tianhe new generation supercomputer. The funders had no role in study design, data collection and analysis, decision to publish, or preparation of the manuscript. The devices were fabricated using the transfer platform from Shanghai Onway Technology Co., Ltd.

AUTHOR CONTRIBUTIONS

Z. H., X. Z., and Y. Z. contributed equally to this work. Z. H. and Y. Z. performed the sample fabrication, characterization, and measurements. X. Z. performed the DFT calculations. Z. H., Y. R., and L. H. analyzed the data. L. H. and Y. R. conceived and provided advice on the experiment and analysis. Y. X. conceived and provided advice on the calculation and analysis. Z. H., X. Z., Y. R., and L. H. wrote the paper with the input from others. All authors contributed to the manuscript and approved the final version.

DECLARATION OF INTERESTS

Lin He is an Editorial Board member of The Innovation Physics and was blinded from reviewing or making final decisions on the manuscript. Peer review was handled independently of this member and their research group. The other authors declare no conflicts of interest.

DATA AND CODE AVAILABILITY

Data are available from the corresponding author upon reasonable request.

SUPPLEMENTAL INFORMATION

It can be found online at https://doi.org/10.59717/j.tip.2026.100008.